THE JOURNAL OF PHYSICAL CHEMISTRY C

Article

pubs.acs.org/JPCC

Mechanism and Kinetics for Reaction of the Chemical Warfare Agent Simulant, DMMP(*g*), with Zirconium(IV) MOFs: An Ultrahigh-Vacuum and DFT Study

G. Wang,[†] C. Sharp,[†] A. M. Plonka,[‡] Q. Wang,[‡] A. I. Frenkel,[‡] W. Guo,[§] C. Hill,[§] C. Smith,[†] J. Kollar,[∥] D. Troya,[†] and J. R. Morris*[,†]

[†]Department of Chemistry, Virginia Tech, Blacksburg, Virginia 24061, United States

[‡]Department of Materials Science and Chemical Engineering, Stony Brook University, Stony Brook, New York 11794, United States

[§]Department of Chemistry, Emory University, Atlanta, Georgia 30322, United States

[∥]Department of Chemistry and Biochemistry, Kennesaw State University, Kennesaw, Georgia 30144, United States

Supporting Information

ABSTRACT: The mechanism and kinetics of interactions between dimethyl methylphosphonate (DMMP), a key chemical warfare agent (CWA) simulant, and Zr_6-based metal organic frameworks (MOFs) have been investigated with in situ infrared spectroscopy (IR), X-ray photoelectron spectroscopy (XPS), powder X-ray diffraction (PXRD), and DFT calculations. DMMP was found to adsorb molecularly to UiO-66 through the formation of hydrogen bonds between the phosphoryl oxygen and the free hydroxyl groups associated with Zr_6 nodes on the surface of crystallites and not within the bulk MOF structure. Unlike UiO-66, the infrared spectra for UiO-67 and MOF-808, recorded during DMMP exposure, suggest that uptake occurs through both physisorption and chemisorption. The XPS spectra of MOF-808 zirconium 3d electrons reveal a charge redistribution following exposure to DMMP. In addition, analysis of the phosphorus 2p electrons following exposure and thermal annealing to 600 K indicates that two types of stable phosphorus-containing species exist within the MOF. DFT calculations, used to guide the IR band assignments and to help interpret the XPS features, suggest that uptake is driven by nucleophilic addition of an OH group to DMMP with subsequent elimination of a methoxy substituent to form strongly bound methyl methylphosphonic acid (MMPA). The rates of product formation indicate that there are likely two distinct uptake processes, requiring rate constants that differ by approximately an order of magnitude. However, the rates of molecular uptake were found to be nearly identical to the rates of reaction, which strongly suggests that the reaction rates are diffusion-limited. The final products were found to inhibit further reactions within the MOFs, and these products could not be thermally driven from the MOFs prior to decomposition of the MOFs themselves.

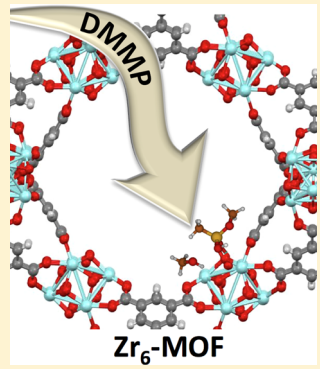

1. INTRODUCTION

The threat of chemical warfare agents (CWAs), assured by their ease of synthesis and effectiveness as a terrorizing weapon, will persist long after the once-tremendous stockpiles in the U.S. and elsewhere are finally destroyed.[1−3] There exists a pressing and continual need for strategies capable of combating these weapons. Soldier and civilian protection, battlefield decontamination, and environmental remediation from CWAs remain top military priorities. As such, new chemical approaches for the fast and complete destruction of CWAs has been an active field of research for many decades, and new technologies, highlighted recently in prominent research journals, have generated immense interest.[4−10] In particular, Zr_6-based metal−organic frameworks (MOFs) have been shown to be active for catalyzing the rapid hydrolysis of chemical warfare nerve agents.[11−17]

MOFs are a class of hybrid organic−inorganic materials with high porosity and extraordinarily large surface areas.[18−21] Some of the most thermal and chemically stable MOFs are constructed from Zr_6-based nodes linked together by carboxylate-terminated struts. The most well-studied example is UiO-66, which consists of $Zr_6(O)_4(OH)_4$ nodes and benzene dicarboxylate linkers.[22] The node connectivity and structure of UiO-66 are illustrated in Figure 1. This MOF has been shown to be stable up to 500 °C, as well as in a variety of organic solvents, acidic solutions, and basic media.[23,24] Perhaps most remarkably, UiO-66 catalyzes the hydrolysis of organophosphorus (OP) nerve agents and nerve agent simulants (less toxic molecular analogues of CWAs) in basic solutions.[12] The catalytic activity of UiO-66 was attributed to the strongly acidic Zr^{IV} ions that are key for the activation of coordinated OP compounds.

Following demonstration of UiO-66 as a catalyst for CWA decomposition, a variety of other Zr_6-based MOFs emerged

Received: January 4, 2017
Revised: April 6, 2017
Published: April 10, 2017

DOI: 10.1021/acs.jpcc.7b00070
J. Phys. Chem. C 2017, 121, 11261−11272

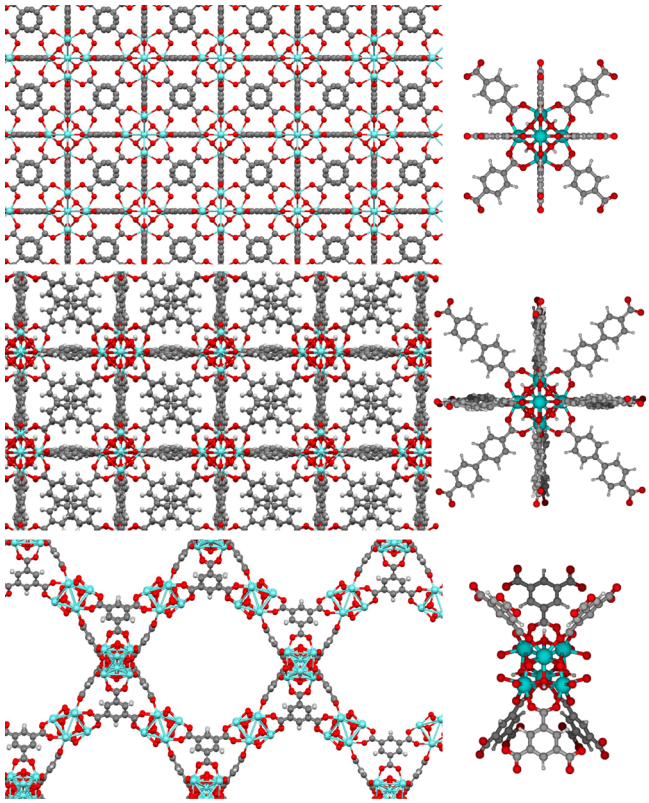

Figure 1. Representations of the UiO-66 (top), UiO-67 (center), and MOF-808 (bottom) MOF structures (left) and their secondary building units (right). Hydrogen atoms in the repeating UiO-66 structure have been omitted for clarity. Atom colors are C: gray, O: red, H: white, Zr: blue.

with much greater turnover frequencies for OP compound hydrolysis. Researchers speculated that the small, 6 Å, pore apertures of UiO-66 (the product of 12 short linkers per node) limit access to the active centers, and thus, catalysis occurs almost exclusively on the external surface of UiO-66.[12] Therefore, several studies pursued Zr_6-based MOFs with more open pore structures. In particular, UiO-67, a 12-connected MOF that is isoreticular to UiO-66 but constructed from extended biphenyl dicarboxylate linkers, was shown to be much more active for OP hydrolysis.[24] The apertures for UiO-67 are 11.5 Å.[24] Researchers hypothesize that hydrolysis occurs at "missing linker" defects within the MOF where substitutionally labile aqua ligands afford the simulants access to the acidic Zr^{IV} ions.[13,25,26]

On the basis of the hypothesis that labile aqua ligands are required for catalyzing OP hydrolysis at Zr_6-MOFs, scientists recently explored these reactions as catalyzed by the six-connected MOF, MOF-808. MOF-808 is composed of the same secondary building unit (SBU) as the UiO series of MOFs but with benzene-1,3,5-tricarboxylate (BTC) serving as the organic linkers. The tricarboxylate groups link three nodes to each ligand, which creates an open-crystalline structure with pores as large as 18 Å.[27−29] Once activated (by removing formate ions that remain from the synthesis), the resulting six-connected nodes have multiple water and hydroxide ligands that decorate the circumference of the nodes (see Figure 1). These ligands, along with the high accessibility of the nodes to the reactants, are likely responsible for the remarkably high decomposition rates of CWA simulants in the presence of this catalyst.

Although, as described above, several Zr_6-based MOFs have been shown to be catalytically active for the hydrolysis of CWAs in aqueous solution, the reactions have yet to be extensively explored for hydrolyzing CWAs or OP simulants in the gas phase. One may hypothesize that the same rapid hydrolysis rates could accompany gas−MOF heterogeneous catalysis. Motivated by both the practical importance of exploring strategies for destroying vaporous CWAs and a fundamental interest in catalysis within MOFs, we have employed ultrahigh-vacuum (UHV)-based surface science methods in a systematic study of organophosphonate−MOF chemistry at the gas−MOF interface. Specifically, infrared spectroscopy has been used to characterize several MOFs and then track bond rupture and formation during exposure of the Zr_6-MOFs to a controlled flux of dimethyl methylphosphonate, a common simulant for the nerve agent sarin. In addition, X-ray photoelectron spectroscopy (XPS) was employed to provide insight into the elemental abundance of the material following exposure and to show how the oxidation state of the nodes is affected by exposure to DMMP. These experimental methods have helped to benchmark parallel computational studies that employed density functional theory (DFT) to map the energetics of initial DMMP binding and subsequent hydrolysis reaction pathways.

2. METHODS

Experiments were performed in an UHV surface science instrument specifically designed to eliminate background contamination, enable a highly controlled flux of a gas of interest onto a particular material, and for in situ monitoring of surface-bound products.[30−34] An instrument base pressure of 10^{-9} Torr ensured that background contamination remained below trace levels throughout the experiment. The MOF samples were prepared by pressing (~60 psi) approximately 15 mg of MOF powder into a 50 μm thick tungsten mesh (Tech-Etch) that could be resistively heated and cooled. During the experiment, the temperature of the sample was monitored by a type-K thermocouple spot-welded adjacent to the sample.

Materials. The samples, UiO-66, UiO-67, and MOF-808, were synthesized according to standard procedures that have been published previously.[24,28] Before being pressed onto the tungsten mesh, the MOFs were activated by solvent exchange with methanol, followed by heating under vacuum at 100 °C for 1 h. After being pressed and loaded into the UHV chamber, the MOFs were further heated to 100 °C for 10 min.

DMMP (97%, purchased from Sigma-Aldrich) was stored in a glass bulb attached to a bellows-sealed valve on a stainless steel gas-handling manifold. A stainless steel directional doser with a capillary array positioned approximately 5 mm from the sample was used to dose DMMP to the sample. A description of the heated manifold and doser can be found in previously published literature.[35] The flux of DMMP for these experiments was estimated to be 3×10^{15} molecules s^{-1} cm^{-2}.

Powder X-ray Diffraction. Prior to the experiments, each MOF was characterized by powder X-ray diffraction (PXRD). All three samples used for further experiments were pure phase as no additional reflections were observed (Figures S1−S3). The unit cell values were in good agreement with those previously published (Table S1), indicating good quality and crystallinity of the samples. The powder XRD measurements were performed with synchrotron X-rays at the 17-BM

DOI: 10.1021/acs.jpcc.7b00070
J. Phys. Chem. C 2017, 121, 11261−11272

beamline at the Advanced Photon Source (APS) at Argonne National Laboratory with the fast and large 2D detector, using a beam of λ = 0.72959 Å, and were analyzed using the GSAS-II software.[36] The unit cell parameters of all three MOFs were obtained from LeBail fitting, where peak shapes were refined with a pseudo-Voigt function and peak asymmetry corrected with Simpson functions using the Jana2006 software.[37] The background was modeled manually using 50 points. The PXRD patterns of UiO-66, UiO-67, and MOF-808 are consistent with those of the ideal structures, as verified by comparison to models.[38−40]

Infrared Spectroscopy. Interactions between DMMP and the MOFs were monitored in real time by a Bruker IFS 66v/S spectrometer in conjunction with a mercury cadmium telluride detector, which were coupled to the UHV chamber via KBr viewports located on either side of the sample. Each of the spectra shown below was the average of 100 scans at a resolution of 2 cm^{-1}, with a 5 mm aperture and 20 kHz scan frequency. The spectra of MOFs in this paper were recorded by using a blank spot on the tungsten mesh as the background, while the clean, pre-exposed MOFs were employed as the background for data presented as difference spectra.

X-ray Photoelectron Spectroscopy. The XPS spectra were recorded using the monochromatic radiation (beam diameter 100 μm, 15 kV) from a Versa Probe III (Physical Electronics). To control charging of the samples, an electron neutralizer (1 eV) and an argon ion gun (10 eV) were used during the measurements. The plots below represent the average of 900 scans for the phosphorus 2p electrons and 30 scans of zirconium 3d electrons.

Computational Methods. All of the DFT calculations employed the M06L functional[41] with an ultrafine integration grid as implemented in the Gaussian09[42] code. Geometry optimizations and harmonic frequencies were obtained with the 6-31G** basis set for main-group elements and the Lanl2dz basis set and pseudopotentials for Zr. The stationary point energies were further refined via addition of diffuse functions in the main-group basis set (6-31++G**). All reported energies in this paper therefore correspond to electronic energies obtained at the M06L/(6-31++G**+Lanl2dz) level, corrected by M06L/(6-31G**+Lanl2dz) zero-point energies. Calculation of sample energies along the lowest-energy reaction path with the larger 6-311++G** basis set (see Table S3) demonstrates small deviations (<5%) from the 6-31++G** results. Therefore, the smaller basis set, which strikes a balance between accuracy and efficiency, is employed throughout this study. Instead of using the 3D MOF structure, a cluster model of the SBU was adopted in this work in which the organic linkers are replaced with formate capping ligands. Previous work on hydrolysis of the larger sarin molecule with UiO-66 showed that explicit consideration of organic linkers in the SBU had a minimal effect on the calculated energies.[60] We therefore expect the cluster model be equally suitable for DMMP in this work.

3. RESULTS AND DISCUSSION

The uptake and decomposition of organophosphonate-based chemical warfare nerve agents within Zr_6-based MOFs have been investigated by tracking the real-time uptake of the more benign simulant molecule, DMMP, within three systems. Specifically, infrared spectroscopy, XPS, and DFT calculations provided insight into how the chemistry of DMMP within UiO-66, UiO-67, and MOF-808 depends on the MOF structure and SBU connectivity. Overall, the results reveal that the UiO-66, with small pore apertures, provides surface sites for physisorption of DMMP but that decomposition does not take place. In contrast, UiO-67 and MOF-808, both with significantly larger pore apertures or channels, provide ample space for DMMP to diffuse into the framework where it reacts to remove hydroxyl groups at the nodes.[24,27,40] The product of the reaction appears to be an irreversibly covalently bound species—the result of nucleophilic addition of a surface OH group to DMMP with subsequent elimination of a methoxy substituent.

Hydrogen Bonding of DMMP on UiO-66. All three MOFs investigated yield rich infrared spectra with narrow bands characteristic of highly crystalline materials. For UiO-66, the IR bands in the low-wavenumber region (Figure 2B, spectrum in black), are well-known to be due to the excitation of vibrational motions associated with the 1,4-benzenedicarboxylate (BDC) linkers, of which there are 12 linkers per node.[43−45] In addition, several features have been previously assigned to collective motions of the node itself.[46] A particularly noteworthy aspect of the infrared spectra is the abundance of bands in the mid-IR range from 1800 to 2700 cm^{-1} (Figure 2A), which are due to overtones and combination bands associated with lower-frequency motions. The high-wavenumber region is characterized by absorbances due to excitation of the C−H stretches around the BDC. The narrow band at 3673 cm^{-1} is assigned to the stretches of the four bridging hydroxyl groups associated with each node (see Figure 1). The band assignments are summarized in Table 1.

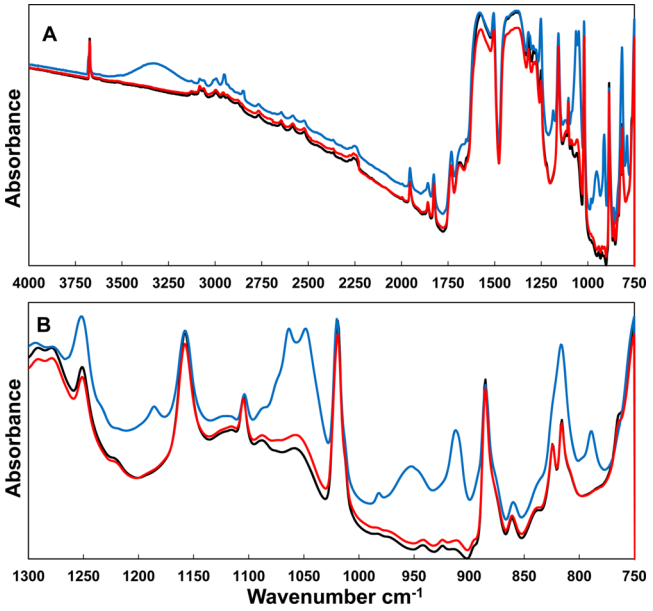

Figure 2. IR spectra for the entire mid-IR region (A) and the "fingerprint" region (B) of UiO-66 before DMMP exposure (black), after DMMP exposure (blue), and after postexposure thermal treatment to 600 K (red).

Upon exposure to DMMP, the infrared bands associated with the UiO-66 remain largely unaffected, but new bands, which can be assigned to the DMMP adsorbate, emerge. The spectra shown in blue in Figures 2A and 2B were recorded following exposure of UiO-66 to 2 × 10^4 L (where 1 L is equivalent to 10^{-6} Torr·s of exposure) of DMMP while the MOF was maintained at 298 K. One of the most significant changes upon exposure is the emergence of a broad band at 3250 cm^{-1}. This

DOI: 10.1021/acs.jpcc.7b00070
J. Phys. Chem. C 2017, 121, 11261−11272

Table 1. Observed Vibrational Wavenumbers (cm^{-1}) for Clean Zr_6-Based MOFs and Band Assignments[46,47,49−59]

mode[a]	UiO-66 cm^{-1}	UiO-67 cm^{-1}	MOF-808 cm^{-1}
ν(ZrO−H)$_{node,free}$	3674	3674	3674
ν(COO−H)$_{linker,free}$		3616	3585
ν(CH)$_{linker}$	3130	3075	3087
	3083	3061	
	3061	3048	
		3015	
overtone	2800−2000	2800−2000	
ν(COZr)$_{bidentate}$ + ν(COO)$_{i.p}$ + ν(C═C) + β(CH)	1662−1520	1638−1471	1646−1500
β(CH)+ν(C═C)	1507		
ν(COZr)$_{bidentate}$ + ν(COO)$_{o.o.p}$ + δ(OH) + β(CH)	1477−1329	1471−1321	1500−1219
ν(C═C) + δ(C═C−C)	1320	1315	
ν(CO)	1300−1260	1269	
ν(C−C) + β(CCH) + δ(OH) + γ(CCC)ϕ χ(ring)		1180	
β(CH) + δ(OH) + χ(ring)	1158	1154	
β(CH) + ν(C═C) + χ(ring)	1105	1121	1112
β(CH) + ν(C═C) + γ(CCC)ϕ χ(ring)		1106	
ν(CO) + δ(OH)	1088		
ν(CO) + δ(OH)	1058		
γ(CCC)ϕ + δ(OH) + χ(ring)	1019	1021	1054
χ(ring) + γ(ring)		1007	942
		974	
		964	
ρ(CH)	885	876	823
	824	856	804
	816	843	
		801	
ν(Zr−O) + γ(CCC)ϕ + ρ(CH)		771	790
ν(Zr−O) + γ(COO)ϕ + ρ(CH)		753	760

[a] ν: bond stretching; ρ: rocking (in-plane); δ: planar angle bending; β: in-plane bending; γ: out-of-plane bending (wagging); ϕ: deformation; χ: aromatic ring breathing; i.p: in-plane; o.o.p: out-of-plane; sh: shoulder.

band, which is accompanied by a reduction in the intensity of the free OH band, is attributed to the formation of a hydrogen bond between DMMP and the hydroxyl groups at the nodes. Previous infrared studies of DMMP (and a variety of other CWA simulants) adsorption on hydroxylated silica demonstrated that DMMP is an excellent hydrogen bond acceptor.[31,32] On silica, the energy of those hydrogen bonds was found to be in excess of 50 kJ/mol.[32] Here, we observe similar types of hydrogen bonding interactions, but they seem to occupy only a small fraction of the total number of free OH groups within the MOF. Note that, even after prolonged exposure, the intensity of the free hydroxyl groups originally present at the nodes was not reduced beyond 20% of the original intensity, implying that the bridging node−OH groups appear to be largely inaccessible to DMMP. The majority of the uptake therefore likely occurs on the surface of the MOF crystallites, and little penetration into the MOF accompanies uptake. This interpretation is consistent with previous suggestions that the pore apertures for UiO-66 are too small for a molecule like DMMP to freely access the interior of the MOF.[12] The aperture size for the octahedral pore is only 12 Å, while that of the tetrahedral pore, where the OH groups reside, is even smaller at 6 Å.[47,48]

The features in the lower-wavenumber region of the spectrum corroborate DMMP physisorption to the MOF through the formation of hydrogen bonds. The many new bands in the region from 750 to 1300 cm^{-1} (Figure 2B) are consistent with prior work into DMMP interfacial hydrogen bonding and can be assigned to molecular DMMP.[16]

Assignment of the bands that emerge upon exposure is aided by a direct comparison to the IR spectrum for gas-phase DMMP (Figure 3). The spectrum shown in blue in Figure 3 was recorded following exposure of UiO-66 to DMMP with the original MOF used as the background such that the new bands represent changes in absorbance due to the vibrational excitations associated with new adsorbates, and negative features are due to changes to bands associated with the original MOF. The resulting difference spectrum for the MOF

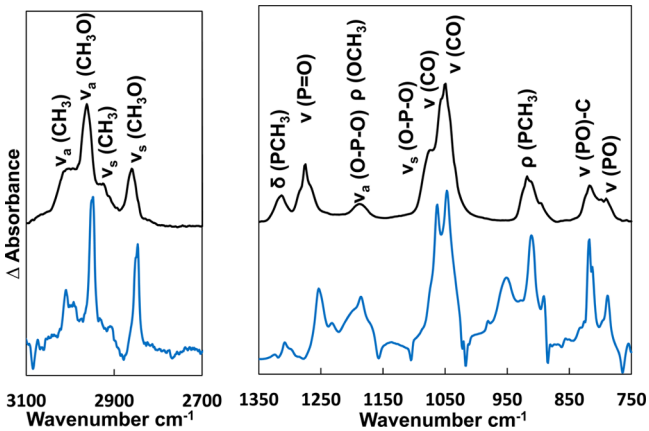

Figure 3. Gas-phase DMMP (black) and difference spectra of DMMP adsorbed onto UiO-66 (blue) at the high-wavenumber region (left) and the low-wavenumber region (right).

DOI: 10.1021/acs.jpcc.7b00070
J. Phys. Chem. C 2017, 121, 11261−11272

upon exposure shows a near 1:1 correlation with the bands for molecular DMMP in the gas phase. This correlation indicates that the types of interactions responsible for DMMP uptake are sufficiently weak that they have little to no effect on the electronic structure of the adsorbate. One notable exception is that the band assigned to the P═O stretch at 1275 cm^{-1} in the gas phase shifts to 1252 cm^{-1} upon adsorption. This shift is consistent with charge redistribution within the P═O bond as some charge transfers to the ZrO−H bond upon hydrogen bond formation (i.e., creation of P═O···HOZr hydrogen bonds). A further indication that the uptake is driven by hydrogen bonding, as opposed to chemistry within the MOF, comes from the absence of significant changes in absorbance of bands originally present in the MOF. That is, the IR data indicate that the framework is largely unaffected by the presence of DMMP.

Following exposure, the MOF was heated to drive off weakly bound adsorbates. The spectra shown in red in Figure 2A and 2B reveal that the original IR spectrum for UiO-66 is recovered following heating. That is, the IR spectra indicate that DMMP thermally desorbs from the UiO-66 and the MOF returns to its original state.

While the current results show that reactivity is below our limit of detection in this UHV-based experiment, we have previously shown that DMMP can access the pores and affect the MOF structure if given sufficient time and exposure. Specifically, under prolonged exposure of UiO-66 to DMMP under atmospheric conditions, the MOF structure was found to measurably change.[17] The difference between the prior work and that described here is related to the level of exposure, 10^4 versus 10^{12} L, which further evidences the very low reaction probability for vaporous DMMP with UiO-66.

Uptake and Reactions of DMMP within UiO-67. The MOF, UiO-67, is isoreticular with UiO-66 but is composed of longer 4,4′ biphenyl-dicarboxylate (BPDC) linkers that expand the pore apertures relative to UiO-66 (to 11.5 Å for tetrahedral and 23 Å for octahedral cavities). The more open structure of UiO-67 therefore provides avenues through which reactants may access the SBUs.[24] Our results demonstrate that the larger pore structure provides reactants with access to sites where chemistry and irreversible binding occur.

Chemisorption of DMMP into UiO-67 is revealed in the IR spectra in Figure 4. The spectrum shown in black in Figure 4 is that of the pristine UiO-67 sample. As for UiO-66, many of the bands for this spectrum have been previously assigned (Table 1). Upon exposure to a controlled flux of gas-phase DMMP (2×10^4 L), several new bands develop in the infrared spectra, while key features in the OH region, assigned to molecular water and free hydroxyl groups, diminish in intensity. However, the bands assigned to linker and node vibrational motions within the MOF remain largely unaffected (see the spectrum shown in blue in Figure 4). Several of the new bands are nearly identical in wavenumber to those assigned to physisorbed DMMP (see the above discussion associated with UiO-66); however, many previously unobserved bands appear in the postexposure IR spectra for UiO-67, suggesting that bond breaking or formation may have accompanied DMMP uptake. Following the room-temperature DMMP exposure, the MOF was heated in an effort to drive the physisorbed molecules from the framework, as was done for the UiO-66 sample. We found that the majority of the new bands for the DMMP-exposed UiO-67 sample that could not be assigned to physisorbed DMMP persisted throughout the thermal annealing procedure

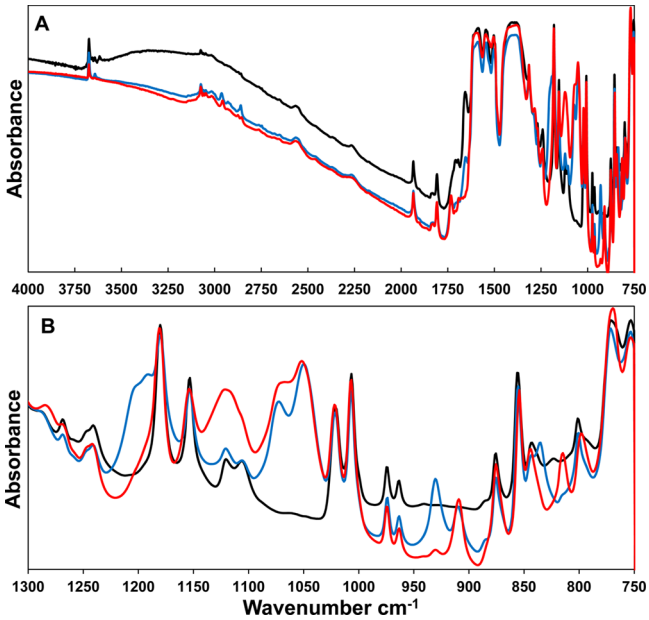

Figure 4. IR spectra for the entire mid-IR region (A) and the "fingerprint" region (B) of UiO-67 before DMMP exposure (black), after DMMP exposure (blue), and after postexposure thermal treatment to 600 K (red).

even when the sample was maintained at 600 K for 60 min (see Figure 4, red). The new bands are hypothesized to be due to the formation of a highly stable chemisorbed methyl methylphosphonic acid (MMPA) species. Many prior studies have shown that DMMP and other organophosphonates react and irreversibly bind at the type of strong Lewis acid sites that may be present at missing-linker defects within the UiO-67 MOF. This hypothesis was tested by repeating the DMMP exposure study with MOF-808, which possesses the same SBU as UiO-67 but is linked by BTCs that produce a very large pore structure and a band of exposed Zr−OH and $Zr-OH_2$ sites that decorate the circumference of the node (see Figure 1).

Uptake and Reactions of DMMP within MOF-808. As described in the Introduction, MOF-808 has been shown to be one of the most effective MOF-based catalysts for the hydrolysis of organophosphonates in buffered solution.[27] Previous studies attribute the high activity of MOF-808 to an open-pore structure, the consequence of only six (as opposed 12 for the UiO-MOFs discussed above) linkers per Zr_6 node.[28] The pore sizes of MOF-808 (18 Å)[27,28] are even larger than those of UiO-67 (11.5 Å).[24] Our results show that MOF-808 reacts irreversibly with the simulant DMMP to produce a significant concentration of node-bound MMPA and methyl phosphonic acid.

Similar to the MOFs described above, the infrared spectra of the pristine MOF-808 (Figure 5, black) are rich in spectral bands for both the linkers and the nodes (see Table 1 for assignments). Most notably, MOF-808 exhibits a narrow band at 3675 cm^{-1} indicative of the free hydroxyl groups that complete the coordination sphere of the node Zr atoms and a broad band in the 3600−3100 cm^{-1} range that is likely due to hydrogen-bonded hydroxyl groups and aqua ligands.[32] As described below, these sites are likely initial docking points for DMMP, where the molecules are sequestered through strong hydrogen bonding interactions.

DOI: 10.1021/acs.jpcc.7b00070
J. Phys. Chem. C 2017, 121, 11261−11272

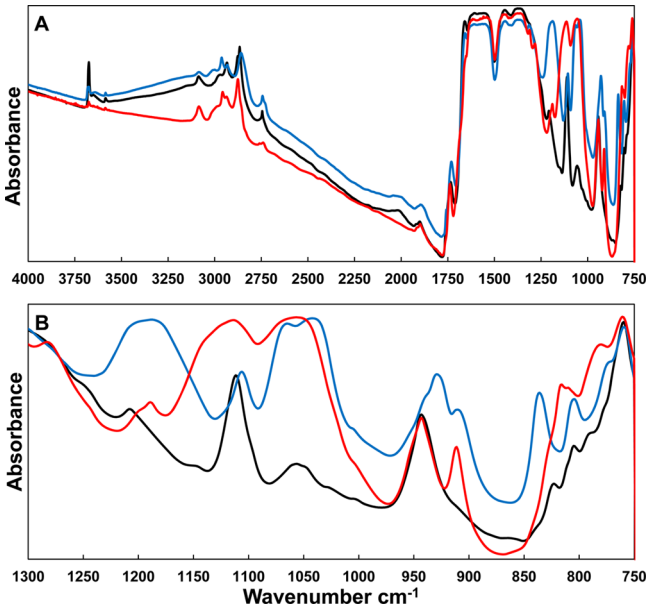

Figure 5. IR spectra for the entire mid-IR region (A) and the "fingerprint" region (B) of MOF-808 before DMMP exposure (black), after DMMP exposure (blue), and after postexposure thermal treatment to 600 K (red).

Upon exposure to DMMP, the free hydroxyl groups diminish in intensity while new bands emerge. The new bands are very similar those described above for exposure to UiO-67 (the detailed difference spectra for MOF-808 and UiO-67 are presented in Figure S4, along with corresponding peak assignments in Table S2). In the C−H region, bands due to physisorbed DMMP as well as chemisorbed methoxy groups develop. These signals are accompanied by the emergence of bands in the low-wavenumber region of the spectrum (Figure 5 B). The strongly chemisorbed species were isolated within the MOF by heating to 600 K, and the resulting IR spectrum following heating is shown by the red trace in Figure 5.

With two broad bands at 1155 cm^{-1} and 1058 cm^{-1} and smaller bands in the 905−750 cm^{-1} region, the difference spectra for MOF-808 and UiO-67 following heating are very similar, suggesting that the same product is formed on each MOF. Figure 6 is a reproduction of the annealed spectra shown in Figures 4 and 5 but with the original MOFs employed as the background such that the primary features in the spectra can be

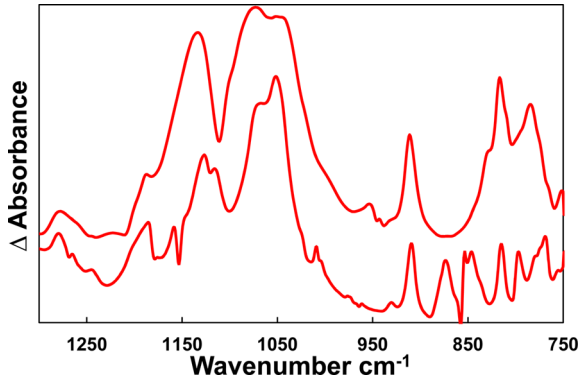

Figure 6. Difference IR spectra of MOF-808 (top) and UiO-67 (bottom) upon DMMP exposure followed by thermal treatment to 600 K for 60 min.

assigned to the MOF-bound reaction products. As the comparison indicates, the adsorbates are strongly bound (i.e., they do not desorb from the MOF even after heating to 600 K) and exhibit similar vibrational spectra for both MOFs.

For both UiO-67 and MOF-808, the most likely MOF-bound product is MMPA, which we hypothesize may bind to the nodes in its deprotonated form following the hydrolysis of DMMP. In fact, recent theoretical work showed that sarin, which has a structure similar to that of DMMP, decomposes to isopropyl methyl phosphonic acid (IMPA) and methyl phosphonofluoridic acid (MPFA) upon reaction with the SBU of UiO-MOFs[60] and another metal-oxide-based cluster, $Cs_8Nb_6O_{19}$.[61] Therefore, we performed energy minimization calculations of a Zr_6 SBU-bound MMPA species. The structure and calculated infrared spectrum, compared to that of the postannealed MOF, are shown in Figure 7. The calculations

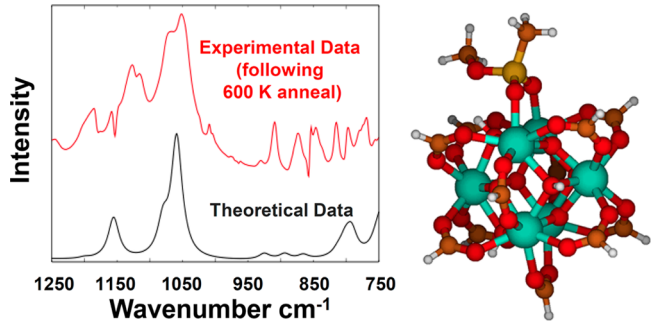

Figure 7. (Left) Experimental (red) difference spectrum and theoretically calculated spectrum (reaction products, black, 10 cm^{-1} line width) of postexposure UiO-67 after thermal treatment at 600 K. (Right) Schematic of the DMMP−UiO-67 reaction product. Color code: Zr: teal, C: brown; P: gold; H: white; O: red.

help assign the O−P−O asymmetric and O−P−O symmetric stretching modes to bands at 1155 and 1058 cm^{-1}, respectively, and the P−C stretching motion is assigned to the band at 791 cm^{-1}, which also agrees with previously published work.[62,63] Together, the experimental and computational results strongly suggest that the irreversibly bound product of DMMP + Zr_6-MOF reactions is MMPA at the SBU.

X-ray Photoelectron Characterization of MOF-Bound Products. While infrared spectra provide insight into the vibrational motions of the MOF-bound species, XPS reveals information about the elemental composition and electronic characteristics of the system. XPS spectra of Zr 3d electrons for MOF-808 before DMMP exposure indicate that the binding energies of Zr $3d_{3/2}$ and Zr $3d_{5/2}$ electrons are 185.61 and 183.27 eV, respectively (Figure 8A). These assignments and binding energies are consistent with previous reports.[64] Upon DMMP exposure, followed by 60 min of thermal treatment at 600 K to remove the physisorbed molecules, the Zr 3d peaks shift slightly to lower binding energy, indicating that the Zr atoms are less positively charged after DMMP reacts with the MOF, which provides evidence for charge redistribution within the node during covalent bond formation with the hypothesized MMPA product.

The XPS spectra for the phosphorus atoms following DMMP exposure to the MOF reveal two binding energy features that suggest that the reaction is more complex than simple MMPA formation. More specifically, upon DMMP exposure to MOF-808, a feature in the photoelectron spectrum

DOI: 10.1021/acs.jpcc.7b00070
J. Phys. Chem. C 2017, 121, 11261−11272

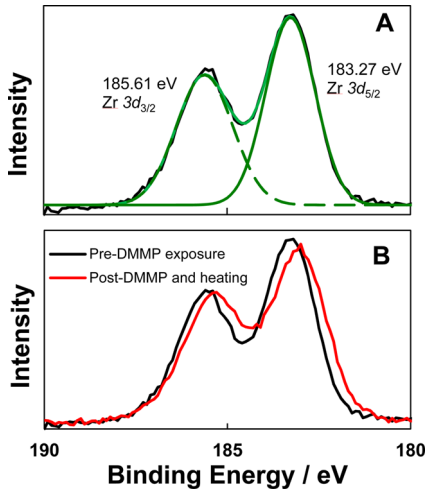

Figure 8. XPS spectra of Zr 3d on MOF-808 before DMMP exposure (A) fitted with two Gaussian components (green) and (B) comparison of the pre-exposed sample to the exposed sample following thermal treatment (600 K).

near 134 eV appears that likely corresponds to the 2p electrons of phosphorus. The P 2p peak can only be adequately modeled with two Gaussian components, which are most likely not due to spin−orbit splitting. That is, not only is the intensity ratio of the peaks inconsistent with spin−orbit splitting of the P 2p electrons, but also the energy difference for these components is only expected to be 0.2 eV, well below that observed here.[65] Therefore, there are likely two types of phosphorus within the MOF, each with a different bonding configuration.

Previous studies into the reaction mechanisms of DMMP on the surface of aluminum, cerium, iron, magnesium, calcium, yttrium, and titanium oxide suggest that multiple phosphorus-containing products form upon uptake. For example, researchers have shown that, at room temperature on Al_2O_3, DMMP losses one methoxy group to form MMPA on the surface, which binds through two O−P bonds. Upon further thermal treatment to near 600 K, part of the MMPA further reacts with the aluminum oxide to shed the other methoxy group and form MPA, which binds to the surface through three O−P bonds. At temperatures below 700 K, MMPA and MPA have been shown to coexist on several of these oxide surfaces.[62,66−71] Upon the basis of the previous studies, we hypothesize that one component of the P 2p XPS spectrum (Figure 9) is due to DMMP molecules that are partially

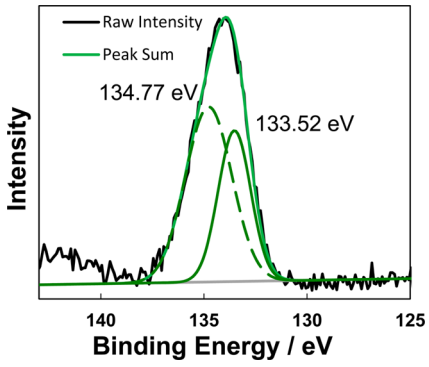

Figure 9. XPS spectra of P 2p on postexposed, thermally treated (600 K) MOF-808 (fitted with two Gaussian components, green).

hydrolyzed (i.e., lose one methoxy group) to form MMPA. The second component may arise from continued reaction of the MMPA product to form MPA. This hypothesis is supported by observation of IR bands that can be assigned to C−H stretching motions for the DMMP-exposed MOF-808 (2924 and 2837 cm^{-1}) and UiO-67 (2927 and 2835 cm^{-1}). The IR and XPS data strongly suggest that one of the products of this reaction is surface methoxides bound to the MOF nodes. These results suggest an overall reaction mechanism that requires initial interactions with Lewis acid sites, which activate the molecule toward nucleophilic attack by water or labile hydroxyl groups. Computational studies have been employed to test this hypothesis.

Computational Studies of the Overall Reaction Pathway. To augment the measurements, we have performed electronic structure calculations of the stationary points of the decomposition reaction of DMMP with the SBU of UiO-66/67. Formally, the decomposition reaction follows a base hydrolysis in which a hydroxide moiety adds nucleophilically to the phosphorus center of DMMP. This addition generates a phosphorus pentacoordinated intermediate that undergoes subsequent elimination of a methanol molecule to yield MMPA.

The reaction occurs at the nodes of the MOFs, which feature a $Zr_6(\mu_3\text{-}O)_4(\mu_3\text{-}OH)_4$ SBU. In UiO-67, the presence of 12 BPDC linkers fully saturates the coordination sphere of the Zr atoms, rendering the node catalytically inactive. Thus, reaction in this MOF occurs at missing linker defects, whose structure has been recently described experimentally[25] and computationally.[26] Removal of one linker generates two adjacent undercoordinated Zr atoms (nodes with several linkers missing would likely present additional undercoordinated reactive Zr atoms). Under ambient conditions and in the most stable configuration, one of these Zr atoms coordinates a hydroxide moiety while the other coordinates a water molecule. A second water molecule is present in the defect and forms hydrogen bonds to both the Zr−OH and $Zr-OH_2$ and a μ_3-OH group in the SBU.[26] In this work, the thermal treatment of the MOFs prior to DMMP exposure likely removes a majority of the coordinated water, leaving a Zr−OH moiety and an adjacent undercoordinated Zr site to which DMMP binds to start the reaction.

Prior computational work has revealed that the most stable binding of DMMP to metal sites is through the O atom of sp^2 hybridization,[72−75] and we have consequently used this binding arrangement to model the interaction of DMMP to the undercoordinated Zr atom of the defective UiO-67 SBU in this work. Within that binding arrangement, there are three possible orientations of the DMMP central tetrahedron with respect to the neighboring Zr−OH moiety that enable reaction. The three orientations differ by the face of the tetrahedron that is approached by the hydroxide nucleophile in the addition step (Figure S5). In two of those orientations, one of the two P−OCH_3 bonds of DMMP is collinear to the forming P−OH bond during nucleophilic addition. In the third orientation, the P−CH_3 bond is collinear to the P−OH bond at the addition transition state. While we have calculated the full reaction pathway in all orientations, Figures 10 and 11 show the potential energy profile and stationary point geometries of the minimum-energy reaction path, which corresponds to a collinear arrangement of the forming P−OH bond and the P−CH_3 group at the addition transition state. Additional geometric detail for this pathway is shown in Figure S6. Energy

DOI: 10.1021/acs.jpcc.7b00070
J. Phys. Chem. C 2017, 121, 11261−11272

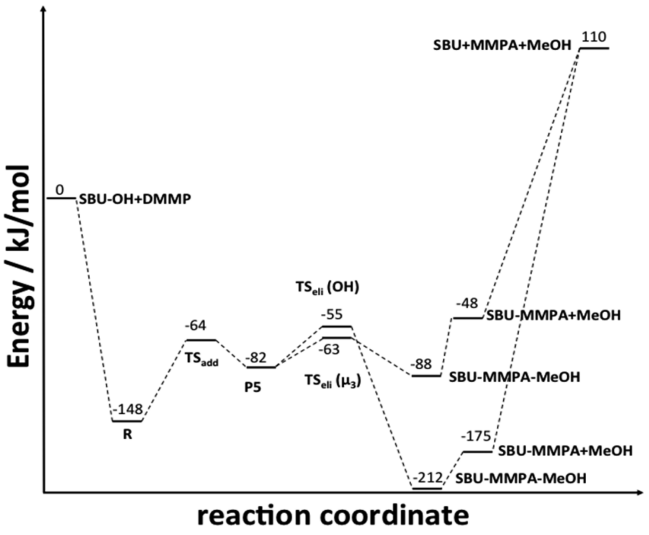

Figure 10. Potential energy profile for the reaction of DMMP with a defective SBU of UiO-67 along the approach in which the P−CH_3 bond of DMMP is collinear to the forming P−OH bond at the addition transition state.

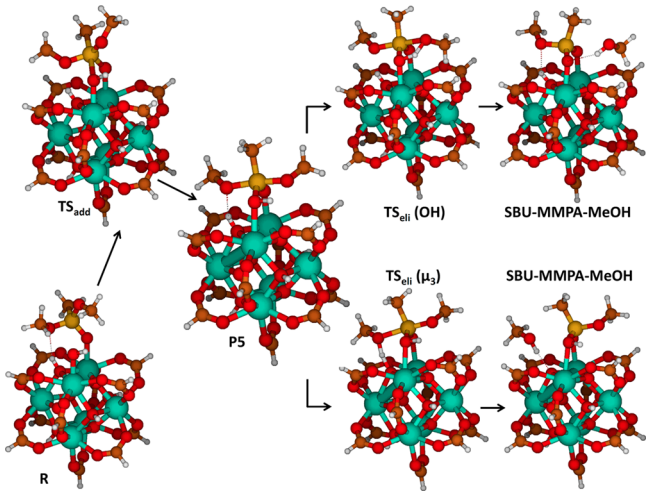

Figure 11. Geometries of the central stationary points in the decomposition of DMMP with a defective SBU of UiO-67 along the approach in which the P−CH_3 bond of DMMP is collinear to the forming P−OH bond at the addition transition state. Same color code as Figure 7.

profiles and structures for the other two orientations are presented in Figures S7−S9.

As mentioned above, reaction starts upon binding of DMMP to the SBU to form a reaction complex (structure R in Figure 11). This binding is exothermic by 148 kJ/mol and coordinates DMMP to a Zr atom adjacent to the Zr−OH group. The first reaction step corresponds to addition of the coordinated OH ligand to the phosphorus atom of DMMP. The transition-state energy for this step is 84 kJ/mol and generates a pentacoordinated phosphorus intermediate (P5). This addition reaction is endothermic by 66 kJ/mol. Proton transfer to the P5 intermediate results in elimination of a methanol molecule and formation of MMPA. There are two elimination pathways, which differ in the source of the proton transferred to the leaving methoxy group. In the lowest-energy elimination pathway, the proton emerges from a μ_3-OH group of the SBU through a barrier of 19 kJ/mol. The second pathway involves proton transfer from the −OH ligand that has mounted the nucleophilic addition and exhibits a slightly larger barrier of 27 kJ/mol. Both elimination pathways yield methanol and MMPA molecules adsorbed on the SBU. Methanol is only bound to the SBU through a hydrogen bond and exhibits desorption energies of ∼40 kJ/mol for the two pathways. Conversely, the MMPA product is strongly bound to the SBU, but the desorption energy depends on the pathway. The elimination process involving proton transfer from the μ_3-OH group generates a protonated MMPA product with two dissimilar Zr−O bond lengths of 2.31 and 2.59 Å, with the longer bond corresponding to the protonated O atom of MMPA. The binding energy of this MMPA product to the SBU is 158 kJ/mol. The proton of the methanol product in the second elimination pathway is transferred from the −OH ligand and generates an aprotic MMPA product that is bound to the SBU in a bidentate manner, with nearly identical Zr−O bond distances of 2.22 and 2.23 Å. MMPA is strongly bound to the SBU, with an enthalpic well depth of 285 kJ/mol relative to the separated products.

The experimental IR spectra in Figure 4 also show the presence of Zr−OCH_3 groups generated during reaction, but the reaction pathways in Figures 11 and S8 and S9 do not provide a source for that moiety. Figure 12 exhibits an alternative reaction pathway that leads to Zr−OCH_3 formation. There are two major differences between this mechanism and the one presented in Figure 11. First, the initial binding of DMMP to the Lewis acid undercoordinated Zr site is through one of the O(sp^3) atoms of DMMP and not through the O(sp^2) atom of the phosphoryl group. The DMMP−MOF binding in Figure 12 is 37.8 kJ/mol weaker than that in Figure 11 but allows for formation of Zr−OCH_3 products. From this binding arrangement, reaction is also initiated via nucleophilic addition of a neighboring Zr−OH group, but elimination of the methoxy moiety occurs directly, without an intervening pentacoordinated phosphorus intermediate. The absence of this intermediate provides the second major difference between the mechanisms in Figures 12 and 11. The products of the

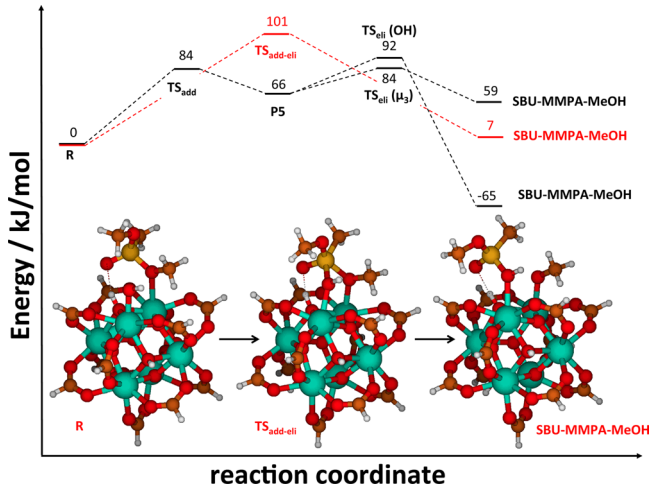

Figure 12. Comparison between the reaction mechanism for decomposition of DMMP on the UiO-67 SBU shown in Figures 10 and 11 (black) and an alternative reaction pathway that results in Zr−OCH_3 formation (red). Energies are referred to the DMMP−MOF reagent complex for each pathway. Insets correspond to reaction along the Zr−OCH_3 pathway. Same color code as Figure 7.

DOI: 10.1021/acs.jpcc.7b00070
J. Phys. Chem. C 2017, 121, 11261−11272

addition−elimination process are a Zr−OCH_3 group and a MMPA product that is bound to the UiO-67 MOF SBU in a monodentate manner and also forms a hydrogen bond with a μ_3-OH group. The barrier for the Zr−OCH_3 formation pathway is only slightly larger than the overall barrier for methanol elimination (Figure 10); therefore, both pathways may play a role in the experiment.

Reaction Kinetics. The kinetics, which provides further insight into the reaction mechanism, was tracked by time-resolved infrared spectra of MOF-808 during DMMP exposure. Upon exposure of the MOF to DMMP, the intensity of the free hydroxyl groups decreases with time, while several new bands simultaneously rise in the low-wavenumber region (see Figure 13). As described above, the consumption of the free hydroxyl groups is integral to decomposition of DMMP into MMPA and MPA; therefore, one may hypothesize that the features assigned to hydroxyl groups should decrease at the same rate as the rise in product bands. The absorbance of the free OH groups has been integrated and plotted versus the exposure time in Figure 14, which also provides the rate of increase for the band at 1175 cm^{-1} (assigned to physisorbed DMMP: the H−C−H and O−C−H bends) and the band at 1050 cm^{-1} assigned to the reaction product, MMPA (O−P−O symmetric stretch in MMPA).

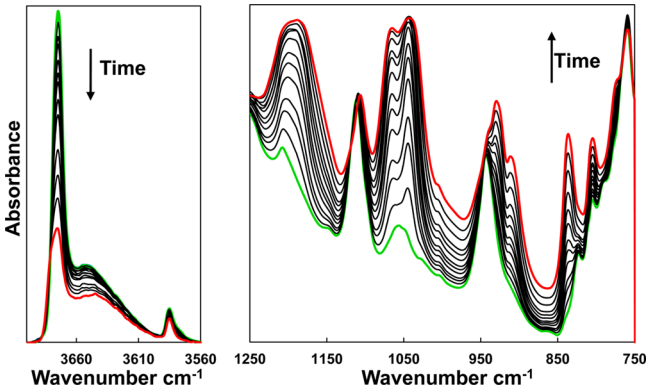

Figure 13. Time-resolved IR spectra are shown for MOF-808 upon DMMP exposure at room temperature (298 K). The high-wavenumber region is shown on the left, and the low-wavenumber region appears on the right. The spectrum in green was recorded before DMMP exposure, and the spectrum in red represents the final spectrum after DMMP exposure.

Clearly depicted in Figure 13 is the fast decrease in intensity for the OH groups accompanied by a similarly rapid rise in bands assigned to MOF adsorbates. The initial changes in band intensities upon exposure of the MOF to DMMP are so rapid relative to the changes at later times that the data cannot be modeled by a single-exponential rise indicative of pseudo-first-order kinetics, as one might expect for a process where impinging molecules react in a single step. Rather, there appear to be two exponential components to the reaction rates. The solid lines in Figure 14 model the data as a sum of two exponential components, and the nonlinear least-squares fitting parameters yield observed rate constants for the various components (see Table 2).

The two rate constants required to adequately describe the kinetics for the development of the main reaction product, MMPA, reveal that there are two reaction pathways. However, the two pathways appear to lead to the same products, as evidenced by the consistency in the wavenumber and bandwidths of these features throughout the experiment (see Figure 13). Therefore, we speculate that the rapid pathway, open at early times, is due to reactions at the most accessible Zr sites and OH groups. The slow reaction component is then due to reactions at sites that are much less accessible, perhaps because they are blocked by the irreversibly bound MMPA products that are generated at short reaction times.

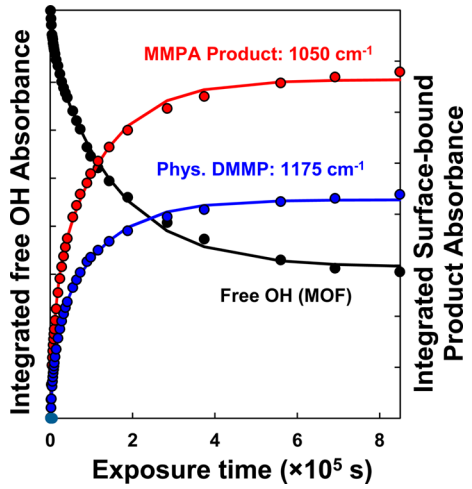

Figure 14. Integrated absorbance of the free OH groups in MOF-808 (black), physisorbed DMMP (blue), and the reaction product (red) versus the DMMP exposure time. The solid lines model the data with two exponential functions that are necessary to capture the fast rise (fall) at early times and the slow development in the data at later times. The fitting parameters are provided in Table 2.

Table 2. Rate Constants (s^{-1}) for the DMMP + MOF-808 Kinetics

component	OH (3674 cm^{-1})	phys. DMMP (1175 cm^{-1})	MMPA (1050 cm^{-1})
fast rise	1.3 (±0.3) × 10^{-3}	8.4 (±2) × 10^{-4}	9.3 (±2) × 10^{-4}
slow plateau	6.3 (±1.3) × 10^{-5}	8.7 (±2) × 10^{-5}	8.3 (±2) × 10^{-5}

Interestingly, the rate of development of the bands assigned to physisorbed DMMP track the rate for OH consumption and product formation. That is, there appear to exist physisorption sites that are both readily accessible and sites that provide some steric hindrance to physisorption. More importantly, the magnitudes of the rate constants are very similar for both DMMP physisorption and DMMP reactions within the MOF. Because the rate of physisorption likely depends primarily on the incident flux and the diffusion rate of DMMP within the MOF, the similarities of the rates for the various components strongly suggest that the reaction rate is diffusion-limited. This observation further supports the mechanism identified by the computational studies, which indicates that the transition states that separate DMMP from the MMPA product have relatively low energies.

4. SUMMARY

The interactions between DMMP and three Zr_6-based MOFs have been explored at a fundamental level through in situ infrared spectroscopy, XPS, and DFT calculations. The interactions between DMMP and UiO-66 appear to be weak and reversible. The infrared spectra show evidence for hydrogen bonding between free hydroxyl groups on the

DOI: 10.1021/acs.jpcc.7b00070
J. Phys. Chem. C 2017, 121, 11261−11272

nodes and DMMP, with the sp^2 oxygen atom of DMMP serving as the primary electron donor; however, the interactions are likely limited to the surface of crystallites rather than within the pore structure of the MOF. In contrast, UiO-67 and MOF-808 are both capable of sequestering DMMP through reversible physisorption and irreversible chemisorption processes. The rates for both processes were found to be very similar, suggesting that the reaction rates for the chemisorption pathway are limited only by the rate of diffusion throughout the MOFs. Calculations suggest that the reaction mechanism consists of nucleophilic attack to the phosphorus atom in the node-bound DMMP by an adjacent Zr−OH group, which ultimately leads to formation of MMPA and methanol or a Zr-bound methoxy. MMPA is strongly bound to the MOF and appears to partially decompose to MPA upon heating.

The results and discussion presented here provide a fundamental framework and experimental benchmarks for future work aimed at elucidating the dynamics of CWA reactions within MOFs. Infrared band assignments and signatures of reactions will aid other work in this area. Importantly, we have shown that open pore structures and the presence of defects are key requirements for building Zr_6-based MOFs that may react with organophosphonate-based CWAs. Finally, the tight binding of the MMPA reaction product at the nodes of open Zr_6-based MOFs may inhibit further chemistry and render these MOFs ineffective as gas-phase catalysts for CWA hydrolysis.

■ ASSOCIATED CONTENT

Supporting Information

The Supporting Information is available free of charge on the ACS Publications website at DOI: 10.1021/acs.jpcc.7b00070.

Powder X-ray diffractograms, IR band assignments, structures of stationary points, and minimum energy reaction paths (PDF)

■ AUTHOR INFORMATION

Corresponding Author

*E-mail: jrmorris@vt.edu. Phone: +1 540 231 2472.

ORCID

C. Sharp: 0000-0002-5313-0760
A. M. Plonka: 0000-0003-2606-0477
A. I. Frenkel: 0000-0002-5451-1207
C. Hill: 0000-0002-5506-9588
D. Troya: 0000-0003-4971-4998
J. R. Morris: 0000-0001-9140-5211

Notes

The authors declare no competing financial interest.

■ ACKNOWLEDGMENTS

This material is based upon work supported by the U.S. Army Research Laboratory and the U.S. Army Research Office under Grant Number W911NF-15-2-0107. This research used resources of the Advanced Photon Source, a U.S. Department of Energy (DOE) Office of Science User Facility operated for the DOE Office of Science by Argonne National Laboratory under Contract No. DE-AC02-06CH11357. The authors are grateful for support of the Defense Threat Reduction Agency. The views and conclusions contained herein are those of the authors and should not be interpreted as necessarily representing the official policies or endorsements, either expressed or implied, of the ARO or the U.S. Government. The U.S. Government is authorized to reproduce and distribute reprints for Governmental purposes notwithstanding any copyright annotation thereon. The authors acknowledge Advanced Research Computing at Virginia Tech for providing computational resources and technical support that have contributed to the results reported within this paper.

■ REFERENCES

(1) *Protocol for the Prohibition of the Use in War of Asphyxiating, Poisonous or Other Gases, and of Bacteriological Methods of Warfare (Geneva Protocol)*; United Nations: Geneva, 1925.

(2) Erickson, R. J. Protocol I: A Merging of the Hague and Geneva Law of Armed Conflict. *Virginia Journal of International Law* **1978**, *19*, 557−594.

(3) Yingling, R. T.; Ginnane, R. W. The Geneva Conventions of 1949. *American Journal of International Law* **1952**, *46*, 393−427.

(4) Yang, Y. C.; Baker, J. A.; Ward, J. R. Decontamination of Chemical Warfare Agents. *Chem. Rev.* **1992**, *92*, 1729−1743.

(5) Stone, H.; See, D.; Smiley, A.; Ellingson, A.; Schimmoeller, J.; Oudejans, L. Surface Decontamination for Blister Agents Lewisite, Sulfur Mustard and Agent Yellow, a Lewisite and Sulfur Mustard Mixture. *J. Hazard. Mater.* **2016**, *314*, 59−66.

(6) Seto, Y. Decontamination of Chemical and Biological Warfare Agents. *Yakugaku Zasshi* **2009**, *129*, 53−69.

(7) Prasad, G. K.; Ramacharyulu, P.; Singh, B. Nanomaterials Based Decontaminants Against Chemical Warfare Agents. *J. Sci. Ind. Res.* **2011**, *70*, 91−104.

(8) Raber, E.; McGuire, R. Oxidative Decontamination of Chemical and Biological Warfare Agents Using L-Gel. *J. Hazard. Mater.* **2002**, *93*, 339−352.

(9) Wagner, G. W. Decontamination of Chemical Warfare Agents Using Household Chemicals. *Ind. Eng. Chem. Res.* **2011**, *50*, 12285−12287.

(10) Talmage, S. S.; Watson, A. P.; Hauschild, V.; Munro, N. B.; King, J. Chemical Warfare Agent Degradation and Decontamination. *Curr. Org. Chem.* **2007**, *11*, 285−298.

(11) Moon, S. Y.; Proussaloglou, E.; Peterson, G. W.; DeCoste, J. B.; Hall, M. G.; Howarth, A. J.; Hupp, J. T.; Farha, O. K. Detoxification of Chemical Warfare Agents Using a Zr-6-Based Metal-Organic Framework/Polymer Mixture. *Chem. - Eur. J.* **2016**, *22*, 14864−14868.

(12) Mondloch, J. E.; Katz, M. J.; Isley, W. C.; Ghosh, P.; Liao, P. L.; Bury, W.; Wagner, G.; Hall, M. G.; DeCoste, J. B.; Peterson, G. W.; et al. Destruction of Chemical Warfare Agents Using Metal-Organic Frameworks. *Nat. Mater.* **2015**, *14*, 512−516.

(13) Moon, S. Y.; Wagner, G. W.; Mondloch, J. E.; Peterson, G. W.; DeCoste, J. B.; Hupp, J. T.; Farha, O. K. Effective, Facile, and Selective Hydrolysis of the Chemical Warfare Agent VX Using Zr-6-Based Metal-Organic Frameworks. *Inorg. Chem.* **2015**, *54*, 10829−10833.

(14) Li, P.; Klet, R. C.; Moon, S. Y.; Wang, T. C.; Deria, P.; Peters, A. W.; Klahr, B. M.; Park, H. J.; Al-Juaid, S. S.; Hupp, J. T.; et al. Synthesis of Nanocrystals of Zr-Based Metal-Organic Frameworks with csq-net: Significant Enhancement in the Degradation of a Nerve Agent Simulant. *Chem. Commun.* **2015**, *51*, 10925−10928.

(15) Katz, M. J.; Mondloch, J. E.; Totten, R. K.; Park, J. K.; Nguyen, S. T.; Farha, O. K.; Hupp, J. T. Simple and Compelling Biomimetic Metal-Organic Framework Catalyst for the Degradation of Nerve Agent Simulants. *Angew. Chem., Int. Ed.* **2014**, *53*, 497−501.

(16) Kanan, S. M.; Tripp, C. P. An Infrared Study of Adsorbed Organophosphonates on Silica: A Prefiltering Strategy for the Detection of Nerve Agents on Metal Oxide Sensors. *Langmuir* **2001**, *17*, 2213−2218.

(17) Plonka, A. M.; Wang, Q.; Gordon, W. O.; Balboa, A.; Troya, D.; Guo, W. W.; Sharp, C. H.; Senanayake, S. D.; Morris, J. R.; Hill, C. L.; et al. In Situ Probes of Capture and Decomposition of Chemical Warfare Agent Simulants by Zr-Based Metal Organic Frameworks. *J. Am. Chem. Soc.* **2017**, *139*, 599−602.

DOI: 10.1021/acs.jpcc.7b00070
J. Phys. Chem. C 2017, 121, 11261−11272

(18) Yaghi, O. M.; Li, H.; Eddaoudi, M.; O'Keeffe, M. Design and Synthesis of an Exceptionally Stable and Highly Porous Metal-Organic Framework. *Nature* **1999**, *402*, 276−279.
(19) Furukawa, H.; Ko, N.; Go, Y. B.; Aratani, N.; Choi, S. B.; Choi, E.; Yazaydin, A. O.; Snurr, R. Q.; O'Keeffe, M.; Kim, J.; et al. Ultrahigh Porosity in Metal-Organic Frameworks. *Science* **2010**, *329*, 424−428.
(20) Eddaoudi, M.; Moler, D. B.; Li, H. L.; Chen, B. L.; Reineke, T. M.; O'Keeffe, M.; Yaghi, O. M. Modular Chemistry: Secondary Building Units As a Basis for the Design of Highly Porous and Robust Metal-Organic Carboxylate Frameworks. *Acc. Chem. Res.* **2001**, *34*, 319−330.
(21) Lee, J.; Farha, O. K.; Roberts, J.; Scheidt, K. A.; Nguyen, S. T.; Hupp, J. T. Metal-Organic Framework Materials as Catalysts. *Chem. Soc. Rev.* **2009**, *38*, 1450−1459.
(22) Valenzano, L.; Civalleri, B.; Chavan, S.; Bordiga, S.; Nilsen, M. H.; Jakobsen, S.; Lillerud, K. P.; Lamberti, C. Disclosing the Complex Structure of UiO-66 Metal Organic Framework: A Synergic Combination of Experiment and Theory. *Chem. Mater.* **2011**, *23*, 1700−1718.
(23) Wu, H.; Yildirim, T.; Zhou, W. Exceptional Mechanical Stability of Highly Porous Zirconium Metal-Organic Framework UiO-66 and Its Important Implications. *J. Phys. Chem. Lett.* **2013**, *4*, 925−930.
(24) Katz, M. J.; Brown, Z. J.; Colon, Y. J.; Siu, P. W.; Scheidt, K. A.; Snurr, R. Q.; Hupp, J. T.; Farha, O. K. A Facile Synthesis of UiO-66, UiO-67 and Their Derivatives. *Chem. Commun.* **2013**, *49*, 9449−9451.
(25) Trickett, C. A.; Gagnon, K. J.; Lee, S.; Gandara, F.; Burgi, H. B.; Yaghi, O. M. Definitive Molecular Level Characterization of Defects in UiO-66 Crystals. *Angew. Chem., Int. Ed.* **2015**, *54*, 11162−11167.
(26) Ling, S. L.; Slater, B. Dynamic Acidity in Defective UiO-66. *Chem. Sci.* **2016**, *7*, 4706−4712.
(27) Moon, S. Y.; Liu, Y. Y.; Hupp, J. T.; Farha, O. K. Instantaneous Hydrolysis of Nerve-Agent Simulants with a Six-Connected Zirconium-Based Metal-Organic Framework. *Angew. Chem., Int. Ed.* **2015**, *54*, 6795−6799.
(28) Li, Z. Q.; Yang, J. C.; Sui, K. W.; Yin, N. Facile Synthesis of Metal-Organic Framework MOF-808 for Arsenic Removal. *Mater. Lett.* **2015**, *160*, 412−414.
(29) Liang, W. B.; Chevreau, H.; Ragon, F.; Southon, P. D.; Peterson, V. K.; D'Alessandro, D. M. Tuning Pore Size in a Zirconium-Tricarboxylate Metal-Organic Framework. *CrystEngComm* **2014**, *16*, 6530−6533.
(30) Zhang, Y. F.; Chapleski, R. C.; Lu, J. W.; Rockhold, T. H.; Troya, D.; Morris, J. R. Gas-Surface Reactions of Nitrate Radicals with Vinyl-Terminated Self-Assembled Monolayers. *Phys. Chem. Chem. Phys.* **2014**, *16*, 16659−16670.
(31) Wilmsmeyer, A. R.; Uzarski, J.; Barrie, P. J.; Morris, J. R. Interactions and Binding Energies of Dimethyl Methylphosphonate and Dimethyl Chlorophosphate with Amorphous Silica. *Langmuir* **2012**, *28*, 10962−10967.
(32) Wilmsmeyer, A. R.; Gordon, W. O.; Davis, E. D.; Troya, D.; Mantooth, B. A.; Lalain, T. A.; Morris, J. R. Infrared Spectra and Binding Energies of Chemical Warfare Nerve Agent Simulants on the Surface of Amorphous Silica. *J. Phys. Chem. C* **2013**, *117*, 15685−15697.
(33) Abelard, J.; Wilmsmeyer, A. R.; Edwards, A. C.; Gordon, W. O.; Durke, E. M.; Karwacki, C. J.; Troya, D.; Morris, J. R. Adsorption of Substituted Benzene Derivatives on Silica: Effects of Electron Withdrawing and Donating Groups. *J. Phys. Chem. C* **2016**, *120*, 13024−13031.
(34) Abelard, J.; Wilmsmeyer, A. R.; Edwards, A. C.; Gordon, W. O.; Durke, E. M.; Karwacki, C. J.; Troya, D.; Morris, J. R. Adsorption of 2-Chloroethyl Ethyl Sulfide on Silica: Binding Mechanism and Energy of a Bifunctional Hydrogen-Bond Acceptor at the Gas Surface Interface. *J. Phys. Chem. C* **2015**, *119*, 365−372.
(35) Yates, J. T., Jr. *Experimental Innovations in Surface Science*; Springer: New York, 2015.
(36) Toby, B. H.; Von Dreele, R. B. GSAS-II: The Genesis of a Modern Open-Source All Purpose Crystallography Software Package. *J. Appl. Crystallogr.* **2013**, *46*, 544−549.
(37) Petříček, V.; Dušek, M.; Palatinus, L. Crystallographic Computing System JANA2006: General Features. *Z. Kristallogr. - Cryst. Mater.* **2014**, *229*, 345−352.
(38) Øien, S.; Wragg, D.; Reinsch, H.; Svelle, S.; Bordiga, S.; Lamberti, C.; Lillerud, K. P. Detailed Structure Analysis of Atomic Positions and Defects in Zirconium Metal−Organic Frameworks. *Cryst. Growth Des.* **2014**, *14*, 5370−5372.
(39) Ko, N.; Hong, J.; Sung, S.; Cordova, K. E.; Park, H. J.; Yang, J. K.; Kim, J. A Significant Enhancement of Water Vapour Uptake at Low Pressure by Amine-Functionalization of UiO-67. *Dalton Transactions* **2015**, *44*, 2047−2051.
(40) Furukawa, H.; Gandara, F.; Zhang, Y. B.; Jiang, J. C.; Queen, W. L.; Hudson, M. R.; Yaghi, O. M. Water Adsorption in Porous Metal-Organic Frameworks and Related Materials. *J. Am. Chem. Soc.* **2014**, *136*, 4369−4381.
(41) Zhao, Y.; Truhlar, D. G. A new local density functional for main-group thermochemistry, transition metal bonding, thermochemical kinetics, and noncovalent interactions. *J. Chem. Phys.* **2006**, *125*, 194101.
(42) Frisch, M. J.; Trucks, G. W.; Schlegel, H. B.; Scuseria, G. E.; Robb, M. A.; Cheeseman, J. R.; Scalmani, G.; Barone, V.; Mennucci, B.; Petersson, G. A.; et al. *Gaussian 09*, revision E.01; Gaussian, Inc.: Wallingford, CT, 2009.
(43) Cliffe, M. J.; Wan, W.; Zou, X. D.; Chater, P. A.; Kleppe, A. K.; Tucker, M. G.; Wilhelm, H.; Funnell, N. P.; Coudert, F. X.; Goodwin, A. L. Correlated Defect Nanoregions in a Metal-Organic Framework. *Nat. Commun.* **2014**, *5*, 8.
(44) Nishida, J.; Tamimi, A.; Fei, H. H.; Pullen, S.; Ott, S.; Cohen, S. M.; Fayer, M. D. Structural Dynamics Inside a Functionalized Metal-Organic Framework Probed by Ultrafast 2D IR Spectroscopy. *Proc. Natl. Acad. Sci. U. S. A.* **2014**, *111*, 18442−18447.
(45) DeCoste, J. B.; Peterson, G. W.; Jasuja, H.; Glover, T. G.; Huang, Y. G.; Walton, K. S. Stability and Degradation Mechanisms of Metal-Organic Frameworks Containing the Zr6O4(OH)(4) Secondary Building Unit. *J. Mater. Chem. A* **2013**, *1*, 5642−5650.
(46) Bensitel, M.; Moraver, V.; Lamotte, J.; Saur, O.; Lavalley, J. C. Infrared Study of Alcohols Adsorption on Zirconium Oxide: Reactivity of Alkoxy Species Towards CO2. *Spectroc. Acta Pt. A-Mol. Biomol. Spectr.* **1987**, *43*, 1487−1491.
(47) Cavka, J. H.; Jakobsen, S.; Olsbye, U.; Guillou, N.; Lamberti, C.; Bordiga, S.; Lillerud, K. P. A New Zirconium Inorganic Building Brick Forming Metal Organic Frameworks with Exceptional Stability. *J. Am. Chem. Soc.* **2008**, *130*, 13850−13851.
(48) Chavan, S.; Vitillo, J. G.; Gianolio, D.; Zavorotynska, O.; Civalleri, B.; Jakobsen, S.; Nilsen, M. H.; Valenzano, L.; Lamberti, C.; Lillerud, K. P.; et al. H-2 Storage in Isostructural UiO-67 and UiO-66 MOFs. *Phys. Chem. Chem. Phys.* **2012**, *14*, 1614−1626.
(49) Sharma, A.; Kaur, S.; Mahajan, C. G.; Tripathi, S. K.; Saini, G. S. S. Fourier Transform Infrared Spectral Study of N,N ′-Dimethylformamide-Water-Rhodamine 6G Mixture. *Mol. Phys.* **2007**, *105*, 117−123.
(50) Yamamoto, H.; Yano, H.; Kouchi, H.; Obora, Y.; Arakawa, R.; Kawasaki, H. N,N-Dimethylformamide-Stabilized Gold Nanoclusters As a Catalyst for the Reduction of 4-Nitrophenol. *Nanoscale* **2012**, *4*, 4148−4154.
(51) Deep, A.; Jain, S.; Sharma, P. C.; Verma, P.; Kumar, M.; Dora, C. P. Design and Biological Evaluation of Biphenyl-4-Carboxylic Acid Hydrazide-Hydrazone for Antimicrobial Activity. *Acta Polym. Pharm.* **2010**, *67*, 255−259.
(52) Tellez S, C. A.; Hollauer, E.; Mondragon, M. A.; Castano, V. M. Fourier Transform Infrared and Raman Spectra, Vibrational Assignment and Ab Initio Calculations of Terephthalic Acid and Related Compounds. *Spectrochim. Acta, Part A* **2001**, *57*, 993−1007.
(53) Lee, M. W.; Kim, M. S.; Kim, K. Infrared and Raman Spectroscopic Study of Terephthalic Acid Adsorbed on Silver Surfaces. *J. Mol. Struct.* **1997**, *415*, 93−100.
(54) Zerbi, G.; Sandroni, S. Fundamental Frequencies and Molecular Configuration of Biphenyl—II Normal Coordinates. *Spectrochimica Acta Part a-Molecular Spectroscopy* **1968**, *24*, 511.

DOI: 10.1021/acs.jpcc.7b00070
J. Phys. Chem. C 2017, 121, 11261−11272

(55) Kaliszewski, M. S.; Heuer, A. H. Alcohol Interaction with Zirconia Powders. *J. Am. Ceram. Soc.* **1990**, *73*, 1504−1509.
(56) Bensitel, M.; Saur, O.; Lavalley, J. C.; Mabilon, G. Acidity of Zirconium Oxide and Sulfated ZrO2 Samples. *Mater. Chem. Phys.* **1987**, *17*, 249−258.
(57) Hertl, W. Surface Chemistry of Zirconia Polymorphs. *Langmuir* **1989**, *5*, 96−100.
(58) Yamaguchi, T.; Nakano, Y.; Tanabe, K. Infrared Study of Surface Hydroxyl Groups on Zirconium Oxide. *Bull. Chem. Soc. Jpn.* **1978**, *51*, 2482−2487.
(59) Dang, Z.; Anderson, B. G.; Amenomiya, Y.; Morrow, B. A. Silica-Supported Zirconia. 1. Characterization by Infrared Spectroscopy, Temperature-Programmed Desorption, and X-ray Diffraction. *J. Phys. Chem.* **1995**, *99*, 14437−14443.
(60) Troya, D. Reaction Mechanism of Nerve-Agent Decomposition with Zr-Based Metal Organic Frameworks. *J. Phys. Chem. C* **2016**, *120*, 29312.
(61) Chapleski, R. C.; Musaev, D. G.; Hill, C. L.; Troya, D. Reaction Mechanism of Nerve-Agent Hydrolysis with the Cs8Nb6O19 Lindqvist Hexaniobate Catalyst. *J. Phys. Chem. C* **2016**, *120*, 16822−16830.
(62) Gordon, W. O.; Tissue, B. M.; Morris, J. R. Adsorption and Decomposition of Dimethyl Methylphosphonate on Y2O3 Nanoparticles. *J. Phys. Chem. C* **2007**, *111*, 3233−3240.
(63) Kuiper, A. E. T.; Vanbokhoven, J.; Medema, J. The Role of Heterogeneity in the Kinetics of a Surface Reaction: I. Infrared Characterization of the Adsorption Structures of Organophosphonates and Their Decomposition. *J. Catal.* **1976**, *43*, 154−167.
(64) Fu, Y. Y.; Yang, C. X.; Yan, X. P. Incorporation of Metal-Organic Framework UiO-66 into Porous Polymer Monoliths to Enhance the Liquid Chromatographic Separation of Small Molecules. *Chem. Commun.* **2013**, *49*, 7162−7164.
(65) Head, A. R.; Tsyshevsky, R.; Trotochaud, L.; Eichhorn, B.; Kuklja, M. M.; Bluhm, H. Electron Spectroscopy and Computational Studies of Dimethyl Methylphosphonate. *J. Phys. Chem. A* **2016**, *120*, 1985−1991.
(66) Templeton, M. K.; Weinberg, W. H. Adsorption and Decomposition of Dimethyl Methylphosphonate on an Aluminum Oxide Surface. *J. Am. Chem. Soc.* **1985**, *107*, 97−108.
(67) Templeton, M. K.; Weinberg, W. H. Decomposition of Phosphonate Esters Adsorbed on Aluminum-Oxide. *J. Am. Chem. Soc.* **1985**, *107*, 774−779.
(68) Kim, C. S.; Lad, R. J.; Tripp, C. P. Interaction of Organophosphorous Compounds with TiO2 and WO3 Surfaces Probed by Vibrational Spectroscopy. *Sens. Actuators, B* **2001**, *76*, 442−448.
(69) Mitchell, M. B.; Sheinker, V. N.; Mintz, E. A. Adsorption and Decomposition of Dimethyl Methylphosphonate on Metal Oxides. *J. Phys. Chem. B* **1997**, *101*, 11192−11203.
(70) Aurianblajeni, B.; Boucher, M. M. Interaction of Dimethyl Methylphosphonate with Metal Oxides. *Langmuir* **1989**, *5*, 170−174.
(71) Chen, D. A.; Ratliff, J. S.; Hu, X. F.; Gordon, W. O.; Senanayake, S. D.; Mullins, D. R. Dimethyl Methylphosphonate Decomposition on Fully Oxidized and Partially Reduced Ceria Thin Films. *Surf. Sci.* **2010**, *604*, 574−587.
(72) Bermudez, V. M. Quantum-Chemical Study of the Adsorption of DMMP and Sarin on Gamma-Al2O3. *J. Phys. Chem. C* **2007**, *111*, 3719−3728.
(73) Bermudez, V. M. Computational Study of Environmental Effects in the Adsorption of DMMP, Sarin, and VX on gamma-Al2O3: Photolysis and Surface Hydroxylation. *J. Phys. Chem. C* **2009**, *113*, 1917−1930.
(74) Bermudez, V. M. Ab Initio Study of the Interaction of Dimethyl Methylphosphonate with Rutile (110) and Anatase (101) TiO2 Surfaces. *J. Phys. Chem. C* **2010**, *114*, 3063−3074.
(75) Bermudez, V. M. Computational Study of the Adsorption of Dimethyl Methylphosphonate (DMMP) on the (010) Surface of Anatase TiO2 with and without Faceting. *Surf. Sci.* **2010**, *604*, 706−712.

DOI: 10.1021/acs.jpcc.7b00070
J. Phys. Chem. C 2017, 121, 11261−11272